



Numerical investigation into premixed hydrogen combustion within two-stage porous media burner of 1 kW solid oxide fuel cell system

Tzu-Hsiang Yen¹, Wen-Tang Hong², Yu-Ching Tsai², Hung-Yu Wang², Cheng-Nan Huang², Chien-Hsiung Lee², Bao-Dong Chen¹

¹Refining & Manufacturing Research Institute, CPC Corporation, Chia-Yi City 60036, Taiwan, ROC.

²Institute of Nuclear Energy Research Atomic Energy Council, Taoyuan County 32546, Taiwan, ROC.

Abstract

Numerical simulations are performed to analyze the combustion of the anode off-gas / cathode off-gas mixture within the two-stage porous media burner of a 1 kW solid oxide fuel cell (SOFC) system. In performing the simulations, the anode gas is assumed to be hydrogen and the combustion of the gas mixture is modeled using a turbulent flow model. The validity of the numerical model is confirmed by comparing the simulation results for the flame barrier temperature and the porous media temperature with the corresponding experimental results. Simulations are then performed to investigate the effects of the hydrogen content and the burner geometry on the temperature distribution within the burner and the corresponding operational range. It is shown that the maximum flame temperature increases with an increasing hydrogen content. In addition, it is found that the burner has an operational range of 1.2~6.5 kW when assigned its default geometry settings (i.e. a length and diameter of 0.17 m and 0.06 m, respectively), but increases to 2~9 kW and 2.6~11.5 kW when the length and diameter are increased by a factor of 1.5, respectively. Finally, the operational range increases to 3.5~16.5 kW when both the diameter and the length of the burner are increased by a factor of 1.5.

Copyright © 2010 International Energy and Environment Foundation - All rights reserved.

Keywords: Solid oxide fuel cell, Porous media combustion, Burner design.

1. Introduction

As the world's supply of natural resources dwindles, a requirement has emerged for highly-efficient, environmental-friendly power generation systems. Solid oxide fuel cells (SOFCs), which produce electrical energy by oxidizing a suitable fuel such as hydrogen or methane, represent a feasible solution for meeting this requirement for a wide variety of applications, ranging from simple auxiliary power units to large-scale power generation systems. SOFCs have a high electrical efficiency (40~60%), low emissions, the ability to operate on a wide variety of different fuels, and the potential for implementation in integrated gasification combined cycles (IGCCs) in order to realize SOFC coal-based central power plants [1, 2, 3].

Many experimental SOFC power generation systems have been developed in order to explore the effects of different fuels, fuel rates and operating temperatures on the operational range of real-world SOFCs. For example, the Institute of Nuclear Energy Research (INER), Taiwan, recently developed a 1 kW SOFC system comprising a natural gas reformer, a fuel stack, an after-burner, a fuel heat exchanger and

an air heat exchanger [4]. Within this system, the two-stage porous media after-burner plays a key role in ensuring the complete conversion of the SOFC off gases during nominal operation, supplying heat during the system start up phase, and pre-heating the cathode intake air during long term operation. Compared to conventional combustion systems with free flame burners, porous media burners have a number of significant advantages, including lower emissions, a wider variable dynamic power range, greater combustion stability, and a freer choice of geometry. As a result, porous burners have been used for many applications in recent years, including household and air heating systems, gas turbine combustion chambers, independent vehicle heating systems, steam generators, and so forth.

The problem of combustion within a porous medium has attracted significant interest in the literature. For example, Trimis and Durst [5] conducted two-section porous media zone experiments in which the two sections contained materials with different properties and porosities, and showed that flame stability and low pollutant emissions could be obtained over a wide range of equivalence ratios. In addition, it was shown that a minimum Peclet number of $Pe = 65$ was required to prevent flame quenching within the porous media. Hayashi *et al.* [6] utilized a one-step reaction model to perform three-dimensional analyses of the flows within a two-layer porous burner for household applications. The results provided a useful understanding of the flame stabilization mechanism within the porous matrix. N-heptane was chosen to model the actual fuel and the combustion process was described by the one-step reaction. Tseng [7] performed a numerical investigation into the effects of hydrogen addition on the combustion of methane in a porous media burner, and showed that adding hydrogen in the fuel the lean limit can be further reduced to $\phi=0.26$. The flame speeds of porous media burner are several times as that of free flames. In addition, it was shown that the porous media burner resulted in a thinner flame thickness than a conventional free flame burner.

As computer technology has developed in recent decades, the use of numerical simulation techniques to obtain detailed insights into the combustion mechanisms within porous media has become increasingly common. Although radiation heat transfer plays an important role in solid phase media, its effects are generally approximated when analyzing the combustion phenomenon using numerical techniques. Consequently, a variety of radiation heat transfer models have been proposed, including the Rosseland model for optically thick media [8], the two-flux approximation model [9], the discrete ordinate (DO) method [10-11], and the direct solution of the one-dimensional radiative transfer equation (RTE) [12-13]. Of these various models, the DO model spans the entire range of optical thicknesses, and permits the solution of problems ranging from surface-to-surface radiation to participating radiation in the combustion process. In addition, the model also allows the solution of radiation at semi-transparent walls and has modest computational and memory requirements. Consequently, the DO model is applied in the numerical simulation here.

Compared to experimental methods, numerical simulations provide a more convenient and versatile means of obtaining detailed insights into the characteristic thermofluidic properties of the stack and afterburner components of an SOFC system. Numerical simulations enable the effects of the various operating parameters (e.g. the fuel mix ratio, the stack intake temperature, the afterburner temperature, and so on) to be easily explored such that the optimum operating conditions can be identified. In the present study, numerical simulations are performed to analyze the premixed combustion problem within the two-stage porous media burner in the 1 kW SOFC system developed by INER [4]. In contrast to most previous studies in which methane was used as the fuel, the present simulations consider the fuel (and the anode-off gas) to be hydrogen. To the best of the current authors' knowledge, no generally accepted model exists for turbulent premixed porous media combustion. The validity of the numerical model is confirmed by comparing the results obtained for the flame barrier temperature and the porous media temperature with the corresponding experimental results obtained using the INER SOFC system. Simulations are then performed to investigate the effects of the hydrogen content and the geometry of the porous media burner on the temperature distribution within the burner and the corresponding operational range.

The remainder of this paper is organized as follows. Section 2 describes the mathematical model, numerical method and boundary conditions imposed in the simulations. Section 3 discusses the validation of the simulation model and presents the simulation results. Finally, Section 4 provides some brief concluding remarks.

2. Mathematical model and numerical method

The modeling of hydrogen combustion within a porous media burner is complicated since it requires the solution of a coupled problem involving fluid flow, heat and mass transfer and chemical reactions within both the porous media and the free space regions of the burner. Furthermore, the fluid and solid properties depend on the temperature and concentration of the gas mixture and therefore result in a non-linear system of partial differential equations. Consequently, certain simplifying assumptions are made in performing the present simulations, namely (1) the gas mixture exhibits steady two-dimensional turbulent flow, (2) the incompressible flow and gases conform to the ideal gas law, (3) gas radiation from the fuel/air combustion mixture is negligible, (4) the porous ceramic materials within the burner have homogeneous properties and emit, adsorb and scatter radiation in such a way as to maintain local thermal equilibrium conditions, (5) the porous ceramic materials are inert and have no catalytic effect on the gas mixture, (6) solid and gas become local thermal equilibrium due to the convective heat transfer coefficient is large enough between gas and solid phase, (7) the Dufour and gravity effects are negligible, and (8) the heat dissociation effect is sufficiently small to be ignored.

2.1 Governing equations

Figure 1 presents a schematic illustration of the burner used in the present simulations and indicates the four temperature measuring positions within the experimental burner. As shown, the burner comprises a mixing chamber (Region A), two porous media sections, namely an upstream fine-pore section (i.e. Region B, the flame barrier zone) and a downstream large-pore section (i.e. Region C, the porous media zone), and a free space region (Region D). In performing the simulations, it is assumed that the burner is fitted with cordierite based honeycomb ceramic and SiC based foam ceramic in Regions B and C, respectively, leading to an excellent modulation behavior, a high power density and low emissions. Furthermore, the cordierite ceramic has an open section of 33% and a pore diameter of 0.8 mm to prohibit the flame propagation in the area, while the metal foam has an open section of 87% and a pore size of 10 pores per inch (ppi).

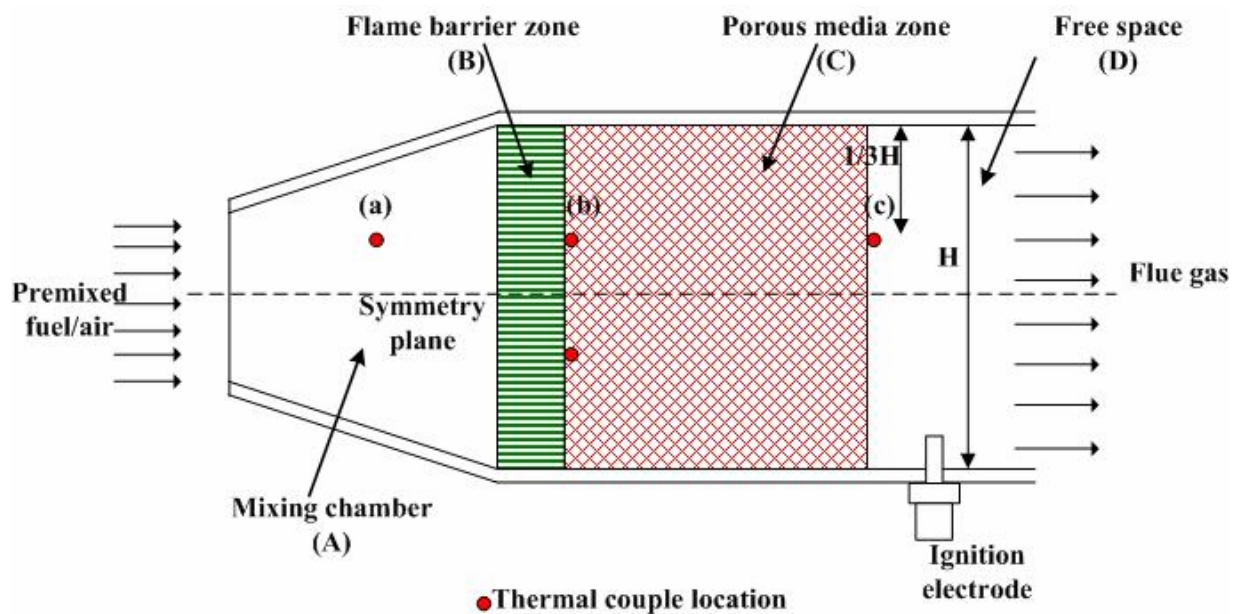


Figure 1. General configuration of two-stage porous media burner

In the simulations, the thermal and turbulent flow fields within the burner are modeled using the turbulent Navier-Stokes and energy equation and are solved numerically using a finite-difference scheme subject to the constraint of satisfying the continuity and species conservation equations. The effects of turbulence are accounted for using an eddy viscosity model, and the flow is assumed to be steady, incompressible, and two-dimensional. In addition, the thermo-physical properties of the solid components within the burner are assumed to be constant. Thus, the governing equation for the gas mixture can be written as follows:

$$\frac{\partial}{\partial x}(\rho u \phi) + \frac{\partial}{\partial y}(\rho v \phi) = \frac{\partial}{\partial x} \left[\Gamma_{\phi} \frac{\partial \phi}{\partial x} \right] + \frac{\partial}{\partial y} \left[\Gamma_{\phi} \frac{\partial \phi}{\partial y} \right] + S_{\phi} \tag{1}$$

where ϕ denotes the dependent variables $u, v, T, k, \varepsilon, Y$; u, v are the local time-averaged velocities in the x - and y -directions respectively; k, ε are the turbulent kinetic energy and turbulent energy dissipation rate, respectively; Y is the mass fraction of the species; and Γ_{ϕ} and S_{ϕ} are the turbulent diffusion coefficient and source term, respectively, for the general variables ϕ . The equations solved in the simulations for the main flow region and porous region of the burner are summarized in Tables 1 and 2, respectively. Note that the empirical constants within the equations used in these regions are assigned values of $C_1 = 1.44, C_2 = 1.92, C_{\mu} = 0.09, \sigma_k = 1.0, \sigma_{\varepsilon} = 1.3$.

Table 1. Summary of equations solved in main flow region of burner

Equations	ϕ	Γ_{ϕ}	S_{ϕ}
Continuity	1	0	0
x – momentum	u	μ_e	$-\frac{\partial p}{\partial x} + \frac{\partial}{\partial x} \left[\mu_e \frac{\partial u}{\partial x} \right] + \frac{\partial}{\partial y} \left[\mu_e \frac{\partial v}{\partial x} \right]$
y – momentum	v	μ_e	$-\frac{\partial p}{\partial y} + \frac{\partial}{\partial x} \left[\mu_e \frac{\partial u}{\partial y} \right] + \frac{\partial}{\partial y} \left[\mu_e \frac{\partial v}{\partial y} \right]$
Energy	T	$\frac{\mu_e}{\sigma_T}$	0
Turbulent energy	k	$\mu_l + \frac{\mu_t}{\sigma_k}$	$-\rho\varepsilon + G$
Turbulent dissipation	ε	$\mu_l + \frac{\mu_t}{\sigma_{\varepsilon}}$	$\frac{\varepsilon}{k}(c_1 G - c_2 \rho \varepsilon)$
Species	Y_i	$\rho D_i + \frac{\mu_t}{Sc_t}$	$M_i = \sum_{r=1}^{N_R} R_{i,r}$

$$G = \mu_t \left\{ 2 \left[\left(\frac{\partial u}{\partial x} \right)^2 + \left(\frac{\partial v}{\partial y} \right)^2 \right] + \left[\frac{\partial u}{\partial y} + \frac{\partial v}{\partial x} \right]^2 \right\}.$$

$$\mu_e = \mu_l + \mu_t.$$

Table 2. Summary of equations solved in porous regions of burner

Equations	ϕ	Γ_ϕ	S_ϕ
Continuity	1	0	0
x – momentum	u	μ_l	$-\nu^2 \frac{\partial p}{\partial x} + (\nu - 1)\mu_l \left[\frac{\partial^2 u}{\partial x^2} + \frac{\partial^2 u}{\partial y^2} \right]$ $- \rho \nu^2 u v \frac{\partial}{\partial y} \left[\frac{1}{\nu} \right] - \frac{\mu_l}{K_p} \nu^2 u - \rho C U \nu^2 u$
y – momentum	v	μ_l	$-\nu^2 \frac{\partial p}{\partial y} + (\nu - 1)\mu_l \left[\frac{\partial^2 v}{\partial x^2} + \frac{\partial^2 v}{\partial y^2} \right]$ $- \rho \nu^2 v v \frac{\partial}{\partial y} \left[\frac{1}{\nu} \right] - \frac{\mu_l}{K_p} \nu^2 v - \rho C U \nu^2 v$
Energy	T	$\frac{\alpha_p}{\rho}$	0
Species	Y_i	ρD_i	$M_i = \sum_{r=1}^{N_R} R_{i,r}$

$$K_p = \frac{d_p^2 \nu^3}{150(1-\nu)^2}.$$

$$C = \frac{1.75}{\sqrt{150\nu^{1.5}}}.$$

$$|U| = \sqrt{u^2 + v^2}.$$

In general, the chemical reaction of the i th species is given by



$$R_{H_2} = AT^\beta [H_2]^b [O_2]^c \exp\left(-\frac{Ea}{R_u T}\right) \quad (3)$$



where $R_{f,r}$ is the forward rate constant for reaction r , R_{H_2} is computed using the Arrhenius expression and A is the pre-exponential factor. The present simulations consider the one-step global forward chemical reaction involved in the hydrogen combustion process. Furthermore, $[H_2]$ and $[O_2]$ denote the concentrations of hydrogen and oxygen, respectively, while parameters b and c are the corresponding concentration exponents. In accordance with [14], the parameters in Eqs. (3) and (4) are specified as $b = 1.1$, $c = 1.1$, $\beta = 0$, $A = 9.87 \times 10^8 \text{ K mol}^{-1.2} \text{ m}^{3.6} \text{ s}^{-1}$, and $Ea = 3.1 \times 10^7 \text{ J / kg mol}$. Simulating the multi-step reaction mechanism in the combustion process involves a significant computational effort. As a result, most previous numerical investigations simplified the reaction process to a single-step chemical reaction. However, the use of a single-step reaction model overstates the flame

temperature and prevents an understanding of the emissions produced by the reaction process. Consequently, Hsu *et al.* [15] argued that it is essential to use multi-step kinetics if accurate predictions of the temperature distribution, energy release rates, and total energy release are required. However, it was also reported in [15] that a single-step kinetics model is adequate for predicting all the flame characteristics other than the emissions for the very lean conditions under which equilibrium favors the more complete combustion process dictated by global chemistry. Table 3 summarizes the compositions of the anode-off and cathode-off gas mixtures considered in the present simulations. The H₂-20 to H₂-8 cases correspond to fuel utilizations in the range $U_f = 0 \sim 0.6$, respectively, and equivalence ratios ranging from 0.27 ~ 0.30. In other words, the present simulations all belong to the lean fuel regime, and can therefore be performed using a single-step reaction model with no significant loss in generality.

Table 3. Compositions of anode-off and cathode-off gas mixtures considered in different simulation runs and corresponding equivalence ratios

Case	H ₂ (slpm)	Air (slpm)	Cooling air (slpm)	H ₂ O (cc/min)	N ₂ (slpm)	Equivalence ratio (ϕ)
H ₂ -20	20	100	76	0	0	0.30
H ₂ -19	19	97.6	76	0.8	1.9	0.29
H ₂ -18	18	95.2	74	1.6	3.8	0.28
H ₂ -17	17	92.9	69	2.4	5.6	0.28
H ₂ -16	16	90.5	63	3.2	7.5	0.28
H ₂ -15	15	88.1	56	4.0	9.4	0.28
H ₂ -14	14	85.7	49	4.8	11.3	0.28
H ₂ -13	13	83.3	43	5.6	13.2	0.28
H ₂ -12	12	81.0	37	6.4	15.0	0.27
H ₂ -11	11	78.6	30	7.2	16.9	0.27
H ₂ -10	10	76.2	23	8.0	18.8	0.27
H ₂ -9	9	73.8	16	8.8	20.7	0.27
H ₂ -8	8	71.4	7	9.6	22.6	0.27

Owing to the high emissivity of the solids in the porous media burner compared to the fluid, the present simulations neglect the effects of gas radiation. However, the divergence of the radiative heat flux from the solids is considered, and is obtained by solving the radiative transfer equation (RTE) using the discrete ordinate (DO) model with the RTE in the direction \vec{s} as a field equation. In general, the RTE for the spectral intensity $I_\lambda(\vec{r}, \vec{s})$ can be written as

$$\nabla \cdot (I_\lambda(\vec{r}, \vec{s})\vec{s}) + (a_\lambda + \sigma_s)I_\lambda(\vec{r}, \vec{s}) = a_\lambda n^2 I_{b\lambda} + \frac{\sigma_s}{4\pi} \int_0^{4\pi} I_\lambda(\vec{r}, \vec{s}') \Phi(\vec{s} \cdot \vec{s}') d\Omega' \quad (5)$$

where λ is the wavelength, a_λ is the spectral absorption coefficient, σ_s is the scattering coefficient, $I_{b\lambda}$ is the black body intensity given by the Planck function, Φ is the phase function, and Ω is the solid angle. In the present simulations, the scattering coefficient, scattering phase function, and refractive index n are all assumed to be independent of the wavelength. Moreover, the porous media are assumed to be gray, homogeneous and isotropically scattering materials. Finally, the extinction and scattering coefficients of the SiC foam are taken from [16].

2.2 Verification of negligible heat dissociation effect

At higher combustion temperatures, the products in the combustion reaction dissociate and form many additional compounds. For example, the compounds produced in hydrogen / oxygen combustion include not only water and nitrogen, but also OH, NO, and CO. Table 4 summarizes the STANJAN calculation results for the molar fractions of the compounds formed in the current combustion process for a hydrogen content of H₂-20 LPM. The results indicate that in the "Equilibrium State" condition, the molar fractions have a very low value for all compounds other than H₂O and N₂. Thus, the validity of assumption #8 in Section 2 (i.e. the heat dissociation effect is negligible) is confirmed.

Table 4. Molar fractions of compounds before and after combustion reaction as determined by STANJAN calculations

Mole Fractions		
	Initial State	Equilibrium State
H ₂	9.8349E-02	2.9956E-08
H	0.0000E+00	2.1673E-10
O	0.0000E+00	7.0006E-08
O ₂	1.6183E-01	1.1832E-01
OH	0.0000E+00	1.0119E-05
H ₂ O	0.0000E+00	1.0343E-01
HO ₂	0.0000E+00	2.6741E-08
H ₂ O ₂	0.0000E+00	2.0832E-09
NO	0.0000E+00	3.1217E-04
NO ₂	0.0000E+00	2.4694E-06
N ₂ O	0.0000E+00	2.0611E-08
HNO	0.0000E+00	9.9136E-12
N ₂	7.3982E-01	7.7792E-01

2.3 Boundary conditions

Figure 2 presents a schematic diagram of the computational domain considered in the present simulations. As shown, a symmetry plane exists along the x-axis of the burner, and thus only a half-model is considered. In performing the simulations, the normal velocity components and variable gradients along the symmetry plane were set to zero, while the remaining boundary conditions were set as described in the following.

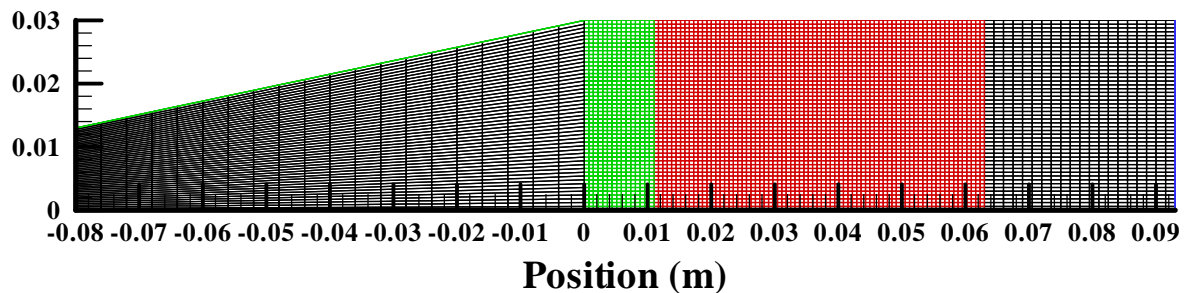


Figure 2. Schematic showing grid distribution within meshed burner

At the inlet of the computational domain, the fuel-air mixture (i.e. the anode-off and cathode-off gas mixture from the SOFC stack) was assumed to have a known temperature T_{mix} specified in accordance with the experimental data presented in [4]. The other boundary conditions at the inlet were specified as follows:

$$u = u_{in}, \quad v = 0, \quad T = T_{mix}, \quad Y_i = Y_{i,in}, \quad q = \pi I_b(T_{mix}) \quad (6)$$

Meanwhile, the boundary conditions at the outlet were specified as

$$\frac{\partial u}{\partial x} = \frac{\partial T}{\partial x} = \frac{\partial Y_i}{\partial x} = 0, \quad q = \pi I_b(T_e) \quad (7)$$

The boundary conditions for the temperature at the outlet were obtained by applying an energy balance between the inlet and outlet boundaries. In addition, the inlet and outlet radiation boundaries in Eqs.(6) and (7) were used to simulate the exchange of radiation with a black body cavity at the burner inlet and outlet temperatures, respectively. Finally, the burner walls were assigned no slip and convection boundary conditions and were assumed to be wrapped with an insulation layer with a thickness of 6 cm. As shown in Fig. 2, the porous media burner was meshed using a non-uniform grid arrangement in order

to reduce the overall computational effort whilst preserving the ability to capture the detailed variations in the temperature distribution within the porous media regions of the burner. The simulations were performed using the SIMPLEC (semi-implicit method for pressure-linked equation consistent) algorithm proposed by Doormaal and Raithby [17]. The algorithm was implemented using pressure and velocity correction schemes in order to ensure a convergent solution in which both the pressure and the velocity satisfied the momentum and continuity equations. Furthermore, an under-relaxation scheme was employed to prevent divergence in the iterative solutions. The resulting sets of discretized equations for each variable were solved using a line-by-line procedure based on the tri-diagonal matrix algorithm (TDMA) and Gauss–Seidel iteration technique presented in Patankar [18]. The solution procedure continued iteratively until the normalized residual of the algebraic equation fell to a value of less than 10^{-4} .

3. Results and discussions

Before commencing the simulations, a grid independence test was performed using three different grid sizes, namely 100 x 10, 100 x 30 and 130 x 50. Figure 3 illustrates the results obtained using the three grid sizes for the temperature profile along the x-axis of the burner at a distance of 1/3H from the burner wall. (Note that the hydrogen content is specified as H₂-20 LPM (see Table 3).) The results show that the numerical solutions are independent of the mesh size for a grid distribution of 130 x 50. Thus, in all the remaining simulations, the grid distribution was specified as 130 x 50.

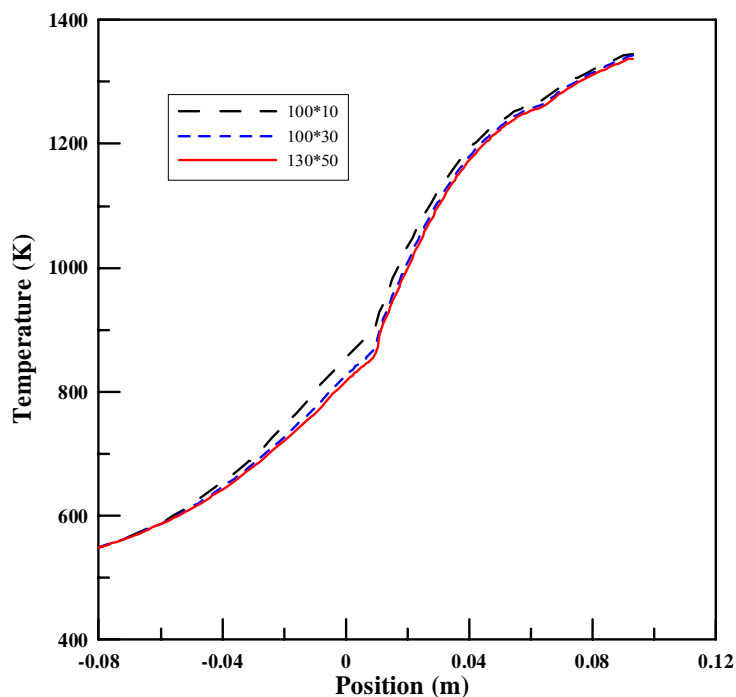


Figure 3. Effect of grid refinement on temperature profile in x-axis direction at distance of 1/3H from burner wall

3.1 Verification of numerical model

In order to verify the numerical model, the simulation results obtained for the flame barrier and porous media temperature for a gas composition from H₂-20 LPM to H₂-8 LPM were compared with the experimental results reported by Yen *et al.* in [4]. The corresponding results are presented in Fig. 4. Note that the flame barrier temperature and porous media temperature data correspond to measurement positions (b) and (c) in Fig. 1, respectively. It is observed that a good agreement exists between the two sets of results for both the flame barrier temperature and the porous media temperature. The discrepancy between the simulation results and the experimental results can be quantified by the error percentage $\frac{(T_{sim} - T_{exp})}{T_{exp}}$. As shown in Fig. 5, the maximum discrepancy between the two sets of results is

found to be just 7% for the flame barrier temperature and 4% for the porous media temperature. Thus, the basic validity of the numerical model is confirmed.

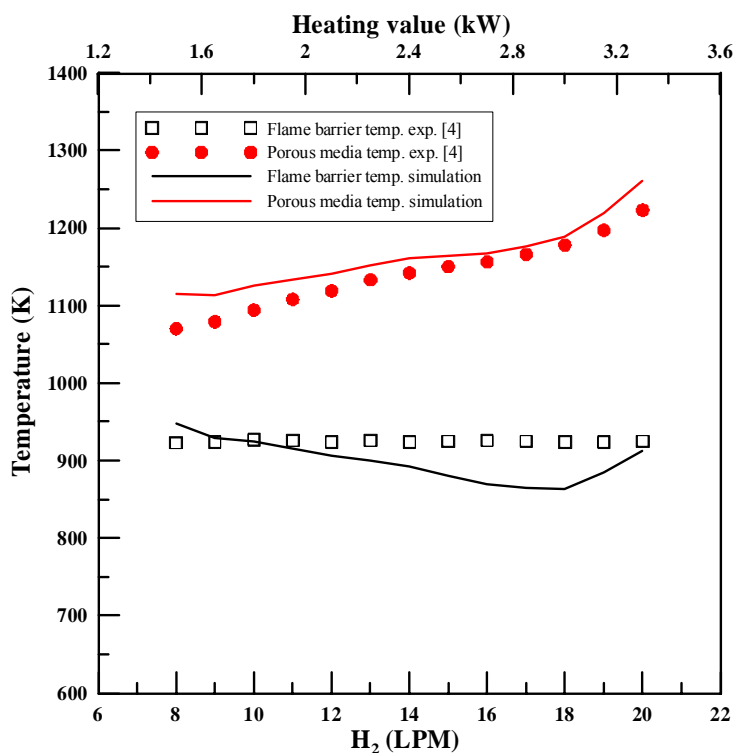


Figure 4. Comparison of experimental and simulation results for flame barrier temperature and porous media temperature at various hydrogen contents in the range H₂-8 ~ H₂-20 LPM

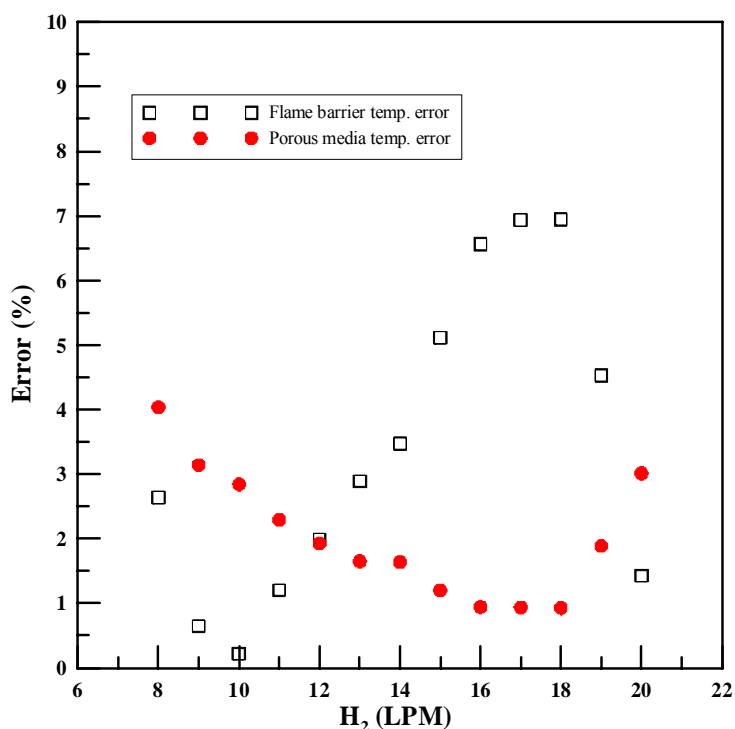


Figure 5. Discrepancy between experimental and simulation results for flame barrier temperature and porous media temperature at various hydrogen contents in the range H₂-8 ~ H₂-20 LPM

3.2 Effect of hydrogen content on temperature distribution within burner

Figures 6(a)~6(g) show the simulated temperature contours within the porous media burner for hydrogen contents of H₂-20~H₂-8 LPM, respectively, corresponding to fuel utilizations of U_f=0~0.6. In general, the flame speed of hydrogen/air mixtures is around 6 times higher than that of methane/air mixtures in free laminar flame burners. Thus, the flame barrier temperature must be carefully controlled in order to

minimize the risk of overheating, flash back or flame extinction. Furthermore, for mixing chamber temperatures greater than 673 K, additional cooling air may be required to prevent flash back [4]. In [4], the mixing chamber temperature in the porous media burner (corresponding to the inlet temperature of the fuel / air mixture in the present simulations) was found to vary between 549 and 664 K under the considered condition. The maximum temperatures in Figs. 6(a)~6(g) are 1354, 1278, 1249, 1234, 1205, 1183, and 1163 K, respectively. Although the equivalence ratios for the seven simulation cases are approximately the same in every case (i.e. 0.27~0.3, see Table 3), the results show that the flame barrier temperature increases with an increasing hydrogen content. Furthermore, it is observed that the maximum temperature within the mixing chamber exceeds a value of 673 K in every case, and thus additional cooling air is required to prevent flash back. The amount of cooling air required increases as the hydrogen content increases and it also results in lower mixing chamber temperature. Finally, it is seen that the anode-off / cathode-off gas mixture entering the mixing chamber pushes the flame position in the downstream direction of the burner. As a result, the maximum temperature is located in the exit region of the burner in every case.

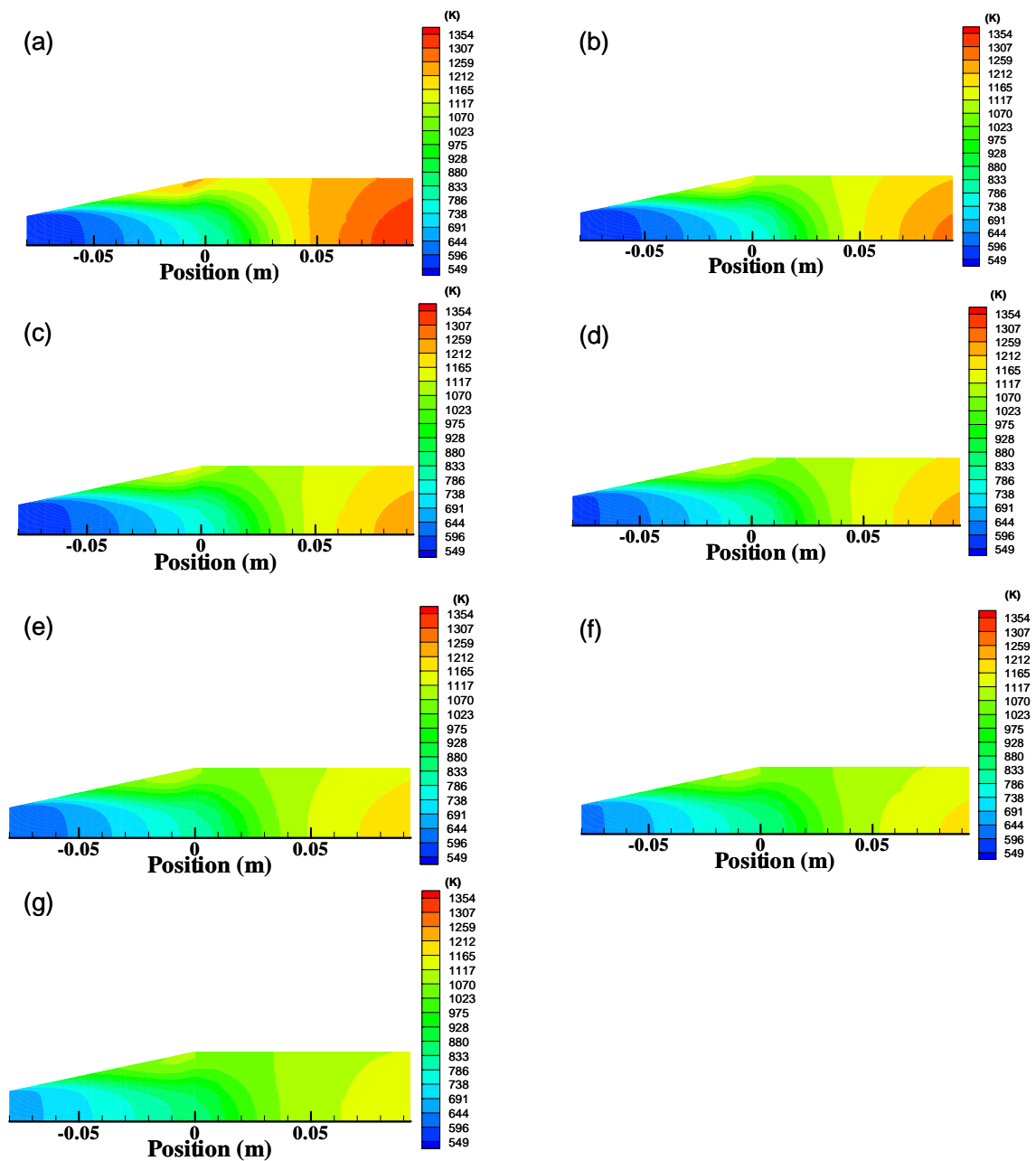


Figure 6. Temperature contours within porous media burner for hydrogen contents of (a) H₂-20, (b) H₂-18, (c) H₂-16, (d) H₂-14, (e) H₂-12, (f) H₂-10, and (g) H₂-8 LPM

Figure 7 illustrates the influence of the hydrogen content (H_2 -8, H_2 -14 and H_2 -20 LPM) on the temperature profile within the porous media regions of the burner. Note that the results correspond to two planes within the burner, namely the central symmetry (SYM) plane and a plane located at a distance of $1/6H$ above the central symmetry plane, respectively. It can be seen that there is little significant difference in the mixture inlet temperature in the various simulation cases. Furthermore, it is apparent that the temperature increases in the downstream direction of the burner for all values of the hydrogen content. However, it is noted that the temperature gradient within the flame barrier zone ($0 \sim 0.011$ m) is lower than that in the porous media zone ($0.011 \sim 0.063$ m). In other words, the different porosity and pore size characteristics of the two porous regions of the burner have a significant effect on the temperature distribution within the burner. Figure 8 presents the temperature distribution along the symmetry plane of the burner for hydrogen contents of H_2 -8 ~ H_2 -20 LPM. As in Fig. 6, the results show that the maximum temperature within the burner increases with an increasing hydrogen content. In addition, it is seen that the difference between the outlet temperature and maximum temperature in region C (i.e. the porous media zone) reduces as the hydrogen content decreases. In other words, for combustion at lower hydrogen concentrations, a more uniform temperature is obtained along the symmetry plane of the burner.

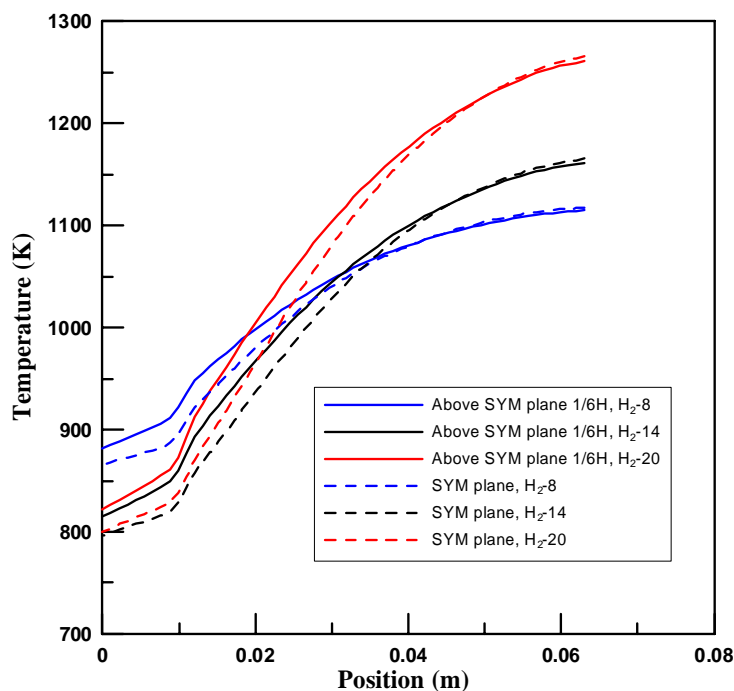


Figure 7. Effect of hydrogen content (fuel utilization) on temperature distribution within porous media regions of burner

Figure 9 illustrates the effect of the hydrogen content on the pattern factor (PF) of the porous media burner. In general, even small variations in the fuel / air mixture ratio of gas turbine combustors can result in measurable, and potentially detrimental, exit thermal gradients. These gradients not only increase the emissions produced by the combustor, but also shorten the design life of any downstream turbomachinery. As a result, a uniform temperature profile is generally sought within the combustor through the careful design and manufacturing of the related combustor components. The pattern factor of the present porous media burner is defined as

$$PF = \frac{T_{out,max} - T_{out,avg}}{T_{out,avg} - T_{in,avg}} \quad (8)$$

where $T_{out,max}$ is the maximum temperature at the burner outlet, $T_{out,avg}$ is the average temperature at the burner outlet, and $T_{in,avg}$ is the average temperature at the burner inlet. Based upon the present

simulation results, the PF value of the porous media burner is found to vary from 0.081 to 0.085. In addition, the PF value is found to increase slightly as the hydrogen content is reduced. Thus, overall, the results reveal that while the exit temperature of the burner is relatively uniform in every case, the uniformity of the temperature distribution reduces slightly as the hydrogen content is decreased.

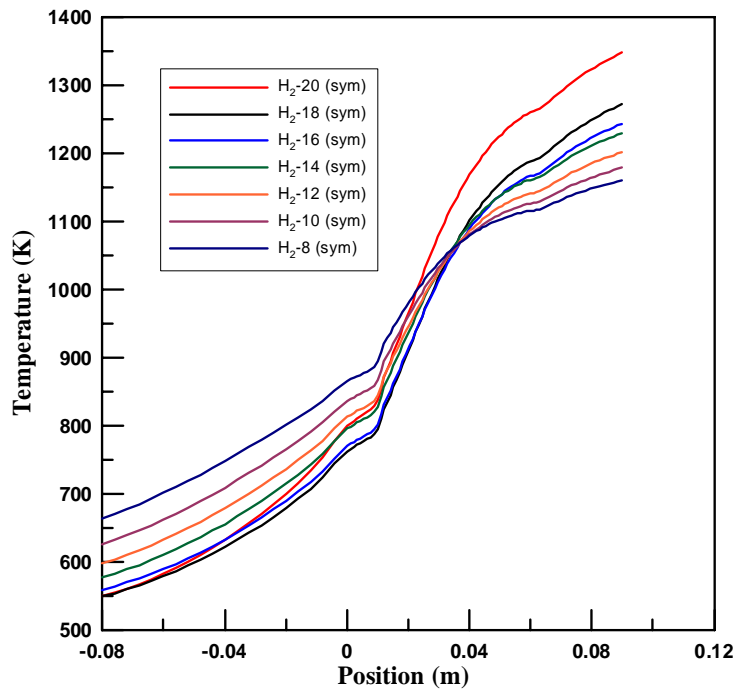


Figure 8. Effect of hydrogen content (fuel utilization) on temperature distribution along burner symmetry plane

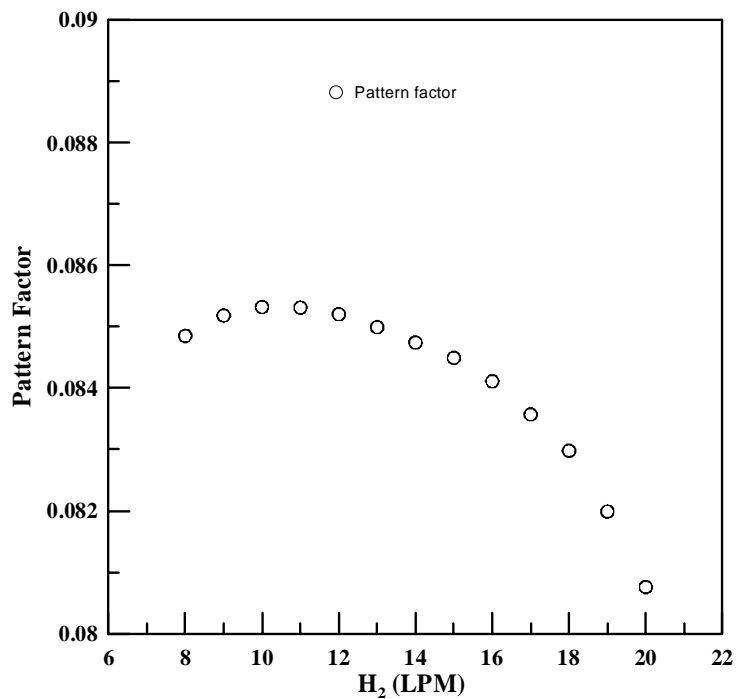


Figure 9. Effect of hydrogen content on pattern factor (PF) of burner

3.3 Effect of burner geometry on operational range

It is well known that the geometry of porous media burners has a significant effect upon the combustion performance. Figure 10 shows the burner geometries considered in the simulations performed in this

study to clarify the geometry effect in the two-stage porous media burner shown in Fig. 1. Specifically, Fig. 10(a) shows the default burner, Fig. 10(b) shows a burner in which the default burner length is increased by a factor of 1.5, Fig. 10(c) shows a burner in which the default diameter is increased by a factor of 1.5, and Fig. 10(d) shows a burner in which both the default length and the default diameter are increased by a factor of 1.5 (i.e. a length and diameter of 0.17 m and 0.06 m, respectively in the original geometry). In establishing the operational range of the two-stage porous media burner, the following conditions apply: (1) the flame barrier temperature should be less than 923 K in order to prevent flash back, (2) the maximum burner temperature should not exceed 1373 K in order to prevent burn out, and (3) the porous media temperature should exceed 1073 K in order to prevent flame extinction [4].

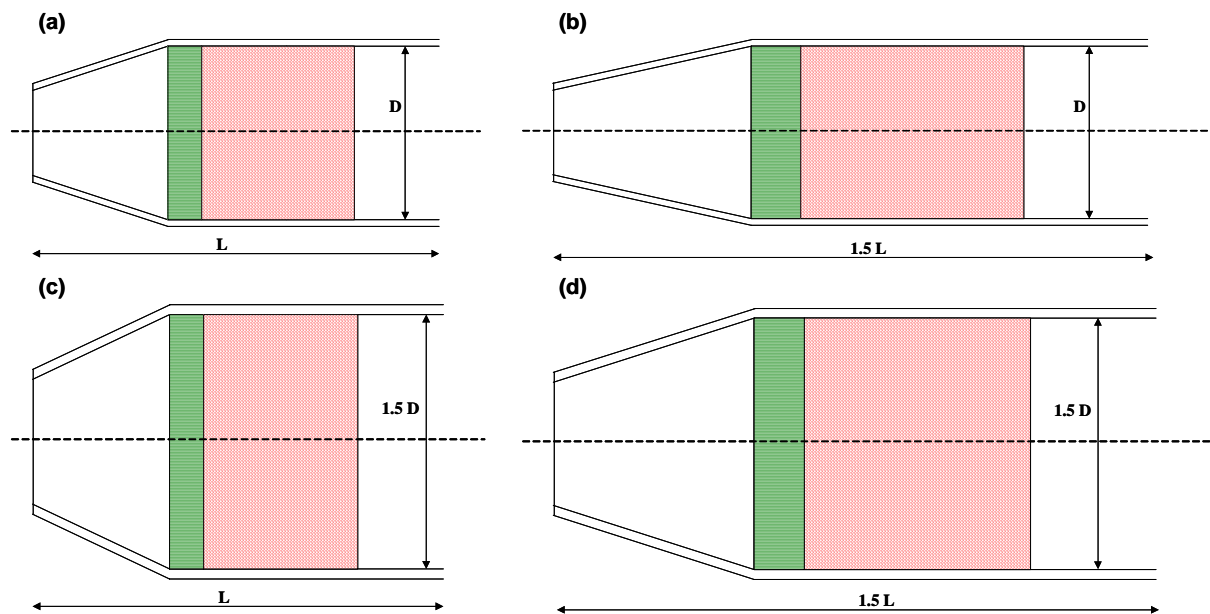


Figure 10. Burner geometries used for comparison purposes in evaluating operational range of burner

For each of the burner geometries shown in Fig. 10, the theoretical operational range can be determined by examining the temperature distributions at the lowest (H_2 -8 LPM) and highest (H_2 -20 LPM) hydrogen concentrations and establishing the flow rate which satisfies the three design constraints given above at each hydrogen concentration. Figs. 6(a) and 6(g) show the temperature contours within the original burner (see Fig. 10(a)) for hydrogen concentrations of H_2 -20 LPM and H_2 -8 LPM, respectively. The corresponding operational range is determined to be 1.2 ~ 6.5 kW. Figure 11 presents the corresponding results for the case in which the burner diameter is unchanged, but the burner length is increased by a factor of 1.5 (see Fig. 10(b)). In this case, the operational range is found to increase to 2 ~ 9 kW. The red dot in the figure is the checking point to satisfy the operation criteria. Figure 12 shows the temperature contours within the burner when the original burner length is unchanged, but the diameter is increased by a factor of 1.5 (see Fig. 10(c)). The corresponding operational range is found to be 2.6 ~ 11.5 kW. Finally, Fig. 13 shows the temperature contours within the burner when both the original burner length and the original burner diameter are increased by a factor of 1.5. In this case, the operational range is found to extend from 3.5 ~ 16.5 kW.

4. Conclusions

This study has performed a numerical investigation into the premixed hydrogen combustion problem within a two-stage porous media burner. In performing the simulations, the flow of the hydrogen / air mixture within the burner has been described using a turbulent flow model and the combustion process has been treated using a simple single-step chemical reaction model. A good agreement has been observed between the simulation results and the experimental results for the flame barrier temperature and porous media temperature at various values of the hydrogen content. Thus, the basic validity of the numerical model has been confirmed. Simulations have been performed to investigate the effects of the hydrogen content and the burner geometry on the temperature distribution within the two-stage burner and the corresponding operational range. It has been shown that the temperature within the burner

increases with an increasing hydrogen content and attains a maximum value in the exit region of the burner. A more uniform temperature distribution is obtained along the symmetry plane of the burner as the hydrogen content reduces. In addition, the rate of temperature increase within the flame barrier zone is lower than that within the porous media zone. The results have confirmed that the operational range of the burner is significantly dependent upon the burner geometry. Specifically, the original burner with a length and diameter of 0.17m and 0.06m, respectively, has an operational range of 1.2~6.5 kW. However, when the burner length or burner diameter is increased by a factor of 1.5, the operational range increases to 2~9 kW and 2.6~11.5 kW, respectively. Finally, when both the burner length and the burner diameter are increased by a factor of 1.5, the operational range increases to 3.5~16.5 kW. Overall, the results presented in this study confirm that the numerical model used in the present simulations yields useful insights into the hydrogen combustion process within a two-stage porous media burner and provides a convenient means of identifying the operating conditions which minimize the risk of flash back or flame extinction.

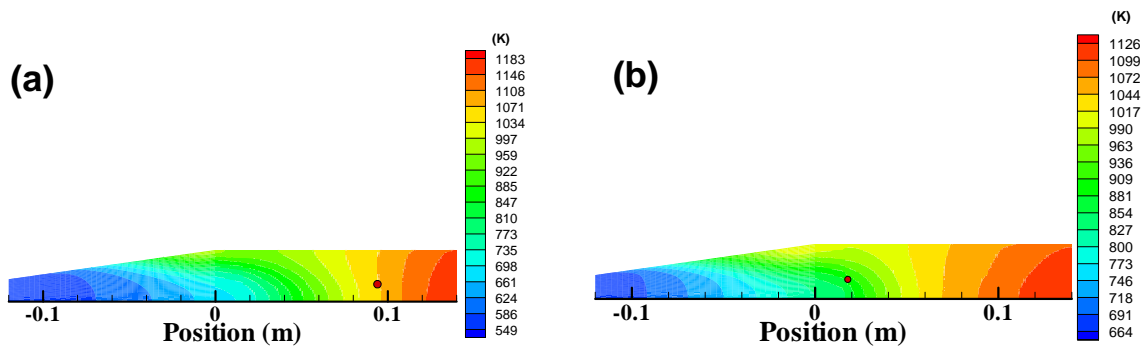


Figure 11. Temperature contours within burner with amplified length (i.e. Figure 10 (b)) under (a) maximum hydrogen content, and (b) lowest hydrogen content conditions

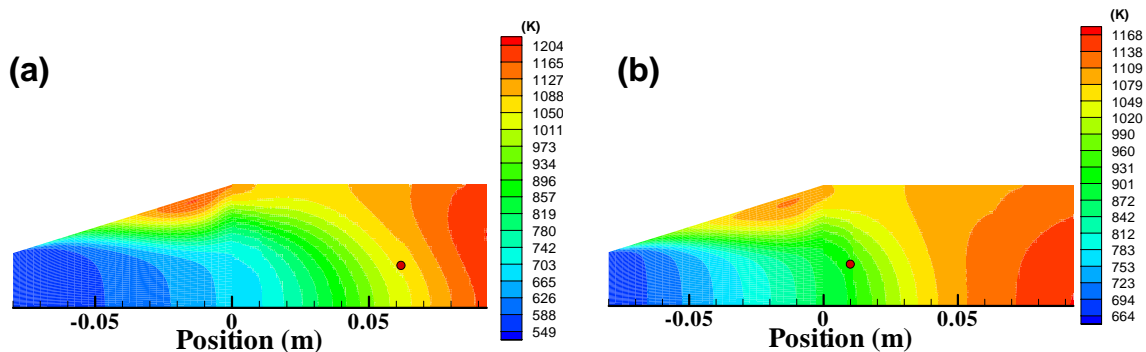


Figure 12. Temperature contours within burner with amplified diameter (i.e. Figure 10 (c)) under (a) highest hydrogen content, and (b) lowest hydrogen content conditions

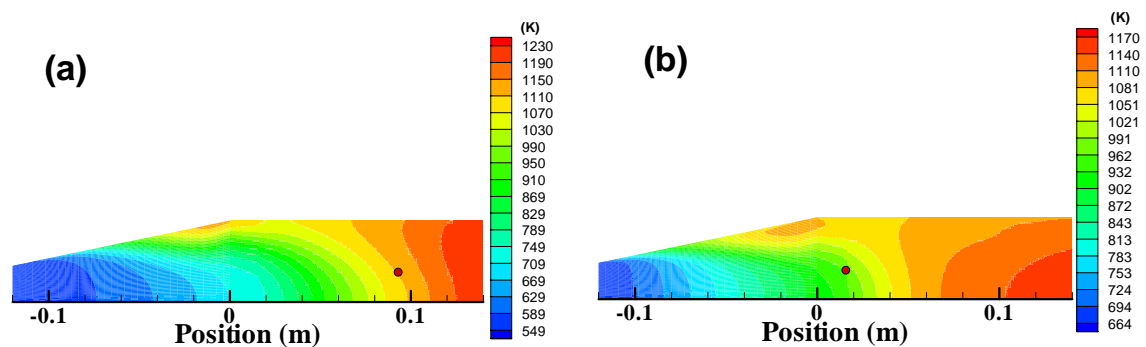


Figure 13. Temperature contours within burner with amplified diameter and amplified length (i.e. Figure 10 (d)) under (a) highest hydrogen content, and (b) lowest hydrogen content conditions

Nomenclature

A	pre-exponential factor
a	spectral absorption coefficient
b	concentration exponent of hydrogen
C_1, C_2, C_μ	turbulent constants
c	concentration exponent of oxygen
Ea	activation energy
I	radiation intensity
k	turbulent kinetic energy (m^2/s^2)
M	species annotation
N	number of chemical species in system
n	refractive index
PF	pattern factor
q	heat flux
R	reaction rate constant
R_u	gas constant
T	temperature (K)
u	velocity in x-direction
v	velocity in y-direction
Y	mass fraction of species

Greek symbols

β	temperature constant
ε	turbulent energy dissipation rate (m^2/s^2)
ρ	density (kg m^{-3})
$\sigma_k, \sigma_\varepsilon$	turbulent constant
σ_s	scattering coefficient
ϕ	equivalence ratio
Ω	solid angle
Φ	phase function
χ	stoichiometric coefficient

Superscripts and subscripts

'	reactant
"	product
b	black body
f	forward
r	rate constant
λ	wavelength
exp	experiment
mix	mixture
sim	simulation

References

- [1] Appleby A. J., Foulker F. R., Fuel Cell Handbook, Van Nostrand Reinhold, New York, 1989.
- [2] Stanley W. A., Direct Energy Conversion, Allyn and Bacon, Inc., Boston, 1982.
- [3] Larminie J., Dicks A., Fuel Cell Systems Explained, John Wiley & Sons, Ltd, England, 2000.
- [4] Yen T. H., Hong W. T., Tsai Y. C., Wang H. Y., Huang W. P., Lee C. H., Experimental investigation of after-burner performance during a SOFC system operation, The 3rd National Conference on Hydrogen Energy and Fuel Cell November 14-15, 2008, Tainan, Taiwan (2008).
- [5] Trimis D., Durst F., Combustion in a Porous Medium - Advances and Applications, Combustion Science and Technology, 121 (1996) 153-168.
- [6] Hayashi T. C., Malico I. and Pereira J. C. F., Three-dimensional modeling of a two-layer porous burner for household applications, Computers and Structures, 82 (2004) 1543-1550.
- [7] Tseng C. J., Effects of hydrogen addition on methane combustion in a porous media burner, International Journal of Hydrogen Energy, 27 (2002) 699-707.
- [8] Mital R., Gore J. P., Viskanta R., A study of the structure of submerged reaction zone in porous ceramic radiant burners, Combustion and flame, 111 (1997) 175-184.
- [9] Rumminger M. D., Dibble R. W., Heberle N. H., Crosley D. R., Gas temperatures above a porous radiant burner. Twenty-Sixth Symposium (International) on Combustion. Pittsburgh: The Combustion Institute, (1997) 1755-1762.
- [10] Zhou X. Y. and Pereira J. C. F., Numerical study of combustion and pollutants formation in inert nonhomogeneous porous media, Combustion Science and Technology, 130 (1997) 335-364.
- [11] Tseng C. J. and Howell J. R., Combustion of Liquid Fuels in a Porous Radiant Burner, Combustion Science and Technology, 112 (1996) 141-161.
- [12] Sathe S. B., Kulkarni M. R., Peck R. E. and Tong T. W., An experimental and theoretical study of porous radiant burner performance, Twenty-third Symposium (International) on Combustion, The Combustion Institute, Pittsburgh, (1990) 1011-1018.
- [13] Yoshizawa Y., Sasaki K. and Echigo R., Analytical Study of the Structure of radiation controlled flame, Journal of Heat and Mass Transfer, 31 (1988) 311-319.
- [14] Ashok K. V., Ashok U. C., Frediano V. B., Studies of premixed hydrogen-air flames using elementary and global kinetics models, Combustion and flame, 64 (1986) 233-236.
- [15] Hsu P. F., Matthews R. D., The necessity of using detailed kinetics in models for premixed combustion within porous media, Combustion and flame, 93 (1993) 457-466.

- [16] Hendricks T. J. and Howell J. R., Absorption/Scattering coefficient and scattering phase functions in reticulated porous ceramics, *Journal of Heat Transfer*, 118 (1996) 79-87.
- [17] Doormaal J.P. van, Raithby F. D., Enhancements of the SIMPLE method for predicting incompressible fluid flows, *Numer. Heat Transfer*, 7 (1984) 147–163.
- [18] Patankar S.V., *Numerical Heat Transfer and Fluid Flow*, McGraw-Hill, New York, 1980.



Tzu-Hsiang Yen obtained a PhD in Mechanical engineering from National Cheng Kung University in Taiwan, 2006. He was a junior researcher at the Institute of Nuclear Energy Research. Now he is working at the Refining and Manufacturing Research Institute, CPC Corporation, Taiwan and responsible for the hydrogen energy planning and research. He has published 15 research papers in reputed International journals and conferences.
E-mail address:078573@cpc.com.tw



Wen-Tang Hong is a senior engineer of Institute of Nuclear Energy Research. He has 19 years research experience, his research topics including: power plant, two phase flow, cold neutron source, and solid oxide fuel cell.
E-mail address:wthang@iner.gov.tw.



Yu-Ching Tsai is an assistant engineer of Institute of Nuclear Energy Research.
E-mail address:engine0316@yahoo.com.tw



Hung-Yu Wang is an assistant engineer of Institute of Nuclear Energy Research.
E-mail address: r92522706@ntu.edu.tw



Cheng-Nan Huang is an assistant engineer of Institute of Nuclear Energy Research.
E-mail address:ahnna@iner.gov.tw



Chien-Hsiung Lee obtained a PhD in nuclear engineering from Purdue University in USA, 1987. He is a senior researcher at the Institute of Nuclear Energy Research. He has been managing the project of solid oxide fuel cell power generating system since 2005. His main research interests include critical heat flux, boiling heat transfer, cold neutron source, and solid oxide fuel cell.
E-mail address:chlee@iner.gov.tw



Bao-Dong Chen holds a PhD degree in chemical engineering from the University of Manchester Institute of Science and Technology (UMIST), UK, in 1992. He is working as Manager of New Energy Department at the Refining and Manufacturing Research Institute, CPC Corporation, Taiwan. Dr Chen has got over 25 years of research and development experience in the refining and petrochemicals industries and published over 30 research papers in reputed national and international journals and conferences.
E-mail address: 929107@cpc.com.tw

